

# Statistical Interior Tomography

Qiong Xu<sup>a</sup>, Hengyong Yu<sup>b,c</sup>, Xuanqin Mou<sup>a</sup>, Ge Wang<sup>c,d</sup>

<sup>a</sup>Institute of Image processing and Pattern recognition, Xi'an Jiaotong University, Xi'an, Shaanxi 710049, P.R.China

<sup>b</sup>Dept. of Radiology, Division of Radiologic Sciences, Wake Forest University Health Sciences, Winston-Salem, NC 27157, USA

<sup>c</sup>Biomedical Imaging Division, VT-WFU School of Biomedical Engineering and Sciences, Wake Forest University Health Sciences, Winston-Salem, NC 27157, USA

<sup>d</sup>Biomedical Imaging Division, VT-WFU School of Biomedical Engineering and Sciences, Virginia Tech., Blacksburg, VA 24061, USA

## ABSTRACT

The long-standing interior problem has been recently revisited, leading to promising results on exact local reconstruction also referred to as interior tomography. To date, there are two key computational ingredients of interior tomography. The first ingredient is inversion of the truncated Hilbert transform with prior sub-region knowledge. The second is compressed sensing (CS) assuming a piecewise constant or polynomial region of interest (ROI). Here we propose a statistical approach for interior tomography incorporating the aforementioned two ingredients as well. In our approach, projection data follows the Poisson model, and an image is reconstructed in the maximum a posterior (MAP) framework subject to other interior tomography constraints including known subregion and minimized total variation (TV). A deterministic interior reconstruction based on the inversion of the truncated Hilbert transform is used as the initial image for the statistical interior reconstruction. This algorithm has been extensively evaluated in numerical and animal studies in terms of major image quality indices, radiation dose and machine time. In particular, our encouraging results from a low-contrast Shepp-Logan phantom and a real sheep scan demonstrate the feasibility and merits of our proposed statistical interior tomography approach.

**Keywords:** Computed tomography (CT), interior tomography, compressed sensing (CS), truncated Hilbert transform, maximum a posterior (MAP) reconstruction

## 1. INTRODUCTION

Reconstruction from the truncated projection data associated with lines through the region-of-interest (ROI) is usually called interior problem, which has been studied for a long time<sup>1-3</sup>. The conventional wisdom is that the interior problem does not have a unique solution<sup>1</sup>. Recently, it has been reported that the interior problem is solvable if some additional prior information is available in advance. This new exactness-oriented local reconstruction methodology is referred to as interior tomography<sup>4</sup>.

To date, there are two key computational ingredients of interior tomography. One ingredient is inversion of the truncated Hilbert transform (THT) with prior sub-region knowledge<sup>5-10</sup>, which is based on the concept of the differentiated back-projection (DBP)<sup>11-13</sup>. Its main idea is to use the analytic continuation technique to extend the known sub-region to the whole ROI. In numerical implementation, first chords/PI-lines are defined passing through the known sub-region, then the DBP along each line is computed, finally certain methods, such as projection onto convex set (POCS)<sup>5,9,13</sup> and singular value decomposition (SVD)<sup>8</sup>, are applied to invert the truncated Hilbert transform (THT) to determine the 1-D image on the line. Another ingredient is compressed sensing (CS) assuming a piecewise constant or polynomial ROI<sup>14-17</sup>. Its main idea is to define an appropriate sparsifying transform and an associated objective function, and then the minimization of the objective function will lead to the true image in ROI. A commonly used sparsifying transform is discrete gradient transform (DGT) and the associated objective function is the sum of DGT, which is usually called total variation (TV), and then the interior ROI can be exactly reconstructed via a TV minimization.

The two aforementioned methods based on THT or CS is exactly for noiseless data when the precise prior knowledge on a subregion in an ROI is known or the ROI is indeed piecewise constant or polynomial<sup>18</sup>. However, these methods did not take into account the statistical nature of projection data, and will not work well in the case of low count data. In fact, the projection measurements should be assumed to obey certain specific statistical distribution<sup>19-21</sup>. Because the well-known statistical iterative reconstruction (SIR) algorithm can accommodate the physical models of data acquisition protocols and demonstrate a better bias-variance performance, it is much more promising than other reconstruction methods.

In this paper, we propose a statistical interior tomography approach to obtain a better performance of interior tomography for practical CT applications. In the next section, we will describe our algorithm scheme. In Section 3, the experimental results for both simulated and real data are shown. Finally, we will discuss the related issues and conclude the paper in the last Section 4.

## 2. METHODOLOGY

In this section, a SIR algorithm will be developed to solve the interior problem. First, we will review the original SIR idea. Then, we describe the CS method for regularization and POCS methods for initialization. These ingredients will be then integrated into our statistical interior tomography scheme.

### 2.1 SIR algorithm

For simplicity, we assume that the x-ray source is monochromatic and the measurements follow a Poisson distribution,

$$y_i \sim \text{Poisson}\{b_i e^{-p_i}\}, \quad i = 1, \dots, N_I, \quad (1)$$

where  $y_i$  is the measurement along the  $i^{\text{th}}$  projection path with  $b_i e^{-p_i}$  being the expected value,  $b_i$  the blank scan factor,  $p_i$  the linear integral of linear attenuation coefficient along the  $i^{\text{th}}$  projection path and  $N_I$  is the number of x-ray paths. For SIR, the object is discretized as rectangular pixels,  $p_i$  can be discretized as follows,

$$p_i = \int_{l_i} \mu(x, y, z) dl \approx \sum_{j=1}^{N_J} a_{ij} \mu_j = [\mathbf{A}\boldsymbol{\mu}]_i, \quad i = 1, \dots, N_I, \quad (2)$$

where  $l_i$  is the x-ray path,  $\mu(x, y, z)$  the linear attenuation coefficient of the material at a 3-D location  $(x, y, z)$ ,  $N_J$  the number of the pixels,  $\mathbf{A} = \{a_{ij}\}$  the system matrix which accounts for the system geometry,  $\boldsymbol{\mu} = (\mu_1, \dots, \mu_{N_J})'$ , and the symbol “'” represents a transpose operator. For the  $i^{\text{th}}$  x-ray path and the  $j^{\text{th}}$  pixel,  $a_{ij}$  can be calculated as the normalized intersection area between the pixel and the ray beam.

Because the measurements along diverse x-ray paths are independent of each other in a statistical sense, the joint probability distribution of the data acquisition process can be expressed as

$$P(\mathbf{y}|\boldsymbol{\mu}) = \prod_{i=1}^{N_I} P(y_i|\boldsymbol{\mu}) = \prod_{i=1}^{N_I} \frac{e^{-\bar{y}_i} \bar{y}_i^{y_i}}{y_i!}, \quad (3)$$

and the corresponding log-likelihood function (ignoring the constant terms) can be written as

$$L(\mathbf{y}|\boldsymbol{\mu}) = \ln P(\mathbf{y}|\boldsymbol{\mu}) = -\sum_{i=1}^{N_I} (y_i p_i + b_i e^{-p_i}) = -\sum_{i=1}^{N_I} (y_i [\mathbf{A}\boldsymbol{\mu}]_i + b_i e^{-[\mathbf{A}\boldsymbol{\mu}]_i}). \quad (4)$$

From the statistical perspective, the original image can be reconstructed by maximizing *a posteriori* (MAP) of function  $P(\boldsymbol{\mu}|\mathbf{y})$ . Since the natural logarithm is monotonically increasing, the maximization of *a posteriori*  $P(\boldsymbol{\mu}|\mathbf{y})$

can be carried out by maximizing its logarithm. According to the Bayesian rule  $P(\boldsymbol{\mu}|\mathbf{y})P(\mathbf{y}) = P(\mathbf{y}|\boldsymbol{\mu})P(\boldsymbol{\mu})$ , the image reconstruction task is equivalent to the maximization of the following objective function

$$\boldsymbol{\mu} = \arg \max_{\boldsymbol{\mu}} \left\{ L(\mathbf{y}|\boldsymbol{\mu}) + \ln P(\boldsymbol{\mu}) \right\}, \quad (5)$$

where  $\ln P(\boldsymbol{\mu})$  expresses the prior knowledge on the object. Because  $\ln P(\boldsymbol{\mu})$  is a regularization term, we denote it as  $R(\boldsymbol{\mu})$  and the objective function can be rewritten as

$$\boldsymbol{\mu} = \arg \min_{\boldsymbol{\mu}} \left\{ \sum_{i=1}^{N_I} \left( y_i [\mathbf{A}\boldsymbol{\mu}]_i + b_i e^{-[\mathbf{A}\boldsymbol{\mu}]_i} \right) + R(\boldsymbol{\mu}) \right\}. \quad (6)$$

Applying a second-order Taylor's expansion to function  $g_i(p) = y_i p + b_i e^{-p}$  around an estimated line integral  $\hat{p}_i = \ln\left(\frac{b_i}{y_i}\right)$ <sup>19</sup>, Eq. (6) can be expressed as

$$\boldsymbol{\mu} = \arg \min_{\boldsymbol{\mu}} \left\{ \sum_{i=1}^{N_I} \frac{y_i}{2} \left( [\mathbf{A}\boldsymbol{\mu}]_i - \hat{p}_i \right)^2 + R(\boldsymbol{\mu}) \right\}. \quad (7)$$

The regularization term  $R(\boldsymbol{\mu})$  usually penalizes the difference among neighboring pixels since the intensities of adjacent pixels are normally similar. A general form of the regularization term is

$$R(\boldsymbol{\mu}) = \beta \sum_{j=1}^{N_J} \sum_{k \in C_j} \omega_{kj} \varphi(\mu_j - \mu_k), \quad (8)$$

where  $\beta$  is an empirical scalar to tradeoff the data fidelity and regularization term,  $\omega_{kj}$  is the weights on differential components,  $C_j$  is the neighborhood of the  $j^{\text{th}}$  pixel, and  $\varphi$  is a potential function that determines the effect of the differential component.

## 2.2 CS method

In the ideal case of noise-free data, the inversion procedure using the CS method can be expressed as follows

$$\min_{\mathbf{u}} \|\Psi \mathbf{u}\|_1, \quad s.t. \quad \Phi \mathbf{u} = \mathbf{b}, \quad (9)$$

where  $\Phi$  is measurement matrix,  $\mathbf{b}$  is the vector of measurements,  $\mathbf{u}$  is the vector of pixels value,  $\Psi \mathbf{u}$  is a sparsifying transform of  $\mathbf{u}$ , and " $\|\cdot\|_1$ " represents the  $\ell_1$  norm. Among all the existing sparsifying transforms, the discrete gradient transform (DGT) is most commonly used. The sum of DGT for each pixel is usually called total variation (TV) of an image. In a 2-D image space, the linear attenuation coefficient  $\mu_j$  of the  $j^{\text{th}}$  pixel can be re-denoted in dual subscripts as

$$\mu_j = \mu_{m,n}, \quad j = (m-1) \times W + n, \quad m = 1, 2, \dots, H, \quad n = 1, 2, \dots, W, \quad (10)$$

where  $W$  and  $H$  are respectively the width and height of the 2-D image array, and  $N_J = W \times H$ . Then, the TV of an image can be expressed as,

$$TV(\boldsymbol{\mu}) = \sum_{m=1}^H \sum_{n=1}^W d_{m,n}, \text{ and } d_{m,n} = \sqrt{(\mu_{m,n} - \mu_{m+1,n})^2 + (\mu_{m,n} - \mu_{m,n+1})^2}. \quad (11)$$

The CS method can be incorporated into the SIR framework in Eq. (7) by substituting  $R(\boldsymbol{\mu})$  with  $\beta \|\Psi \boldsymbol{\mu}\|_1$ . If we choose the DGT as sparsifying transform of an image, we arrive at a CS based SIR framework for minimizing the following objective function

$$\boldsymbol{\mu} = \arg \min_{\boldsymbol{\mu}} \left\{ \sum_{i=1}^{N_I} \frac{y_i}{2} ([\mathbf{A}\boldsymbol{\mu}]_i - \hat{p}_i)^2 + \beta TV(\boldsymbol{\mu}) \right\}. \quad (12)$$

There are various ways to minimize the above objective function. While Tang et al.<sup>22</sup> employed the Gauss-Siedel scheme, in this paper we will use an alternative minimization method in terms of soft-threshold filtering<sup>23</sup>. Therein, for the CS based image reconstruction expressed in Eq. (9), the data fidelity step with the simultaneous algebraic reconstruction technique (SART)<sup>24</sup> and the TV minimization step via soft-threshold filtering are performed in an alternative manner. Similarly, to minimize the objective function Eq. (12), we deal with the log-likelihood term

$\arg \min_{\boldsymbol{\mu}} \left\{ \sum_{i=1}^{N_I} \frac{y_i}{2} ([\mathbf{A}\boldsymbol{\mu}]_i - \hat{p}_i)^2 \right\}$  and the TV term  $\arg \min_{\boldsymbol{\mu}} \{TV(\boldsymbol{\mu})\}$  alternatively. With the separable paraboloid surrogate subject to non-negativity, each update for the log-likelihood term is obtained as follows

$$\mu_j^{n+1} = \left[ \mu_j^n - \frac{\sum_{i=1}^{N_I} (a_{ij} y_i ([\mathbf{A}\boldsymbol{\mu}]_i^n - \hat{p}_i))}{\sum_{i=1}^{N_I} (a_{ij} y_i \sum_{j=1}^{N_J} a_{ij})} \right]_+. \quad (13)$$

### 2.3 Inversion of THT by POCS

When there is a known subregion inside an ROI, the interior problem can be solved by the inversion of THT with the POCS method. First, a set of chord/PI lines are constructed, which go through both the known and unknown regions in the ROI. The linear attenuation coefficient  $\mu(x, y, z)$  on such a chord/PI-line  $L$  is re-denoted as  $f(t)$ , where  $t$  is the 1-D coordinate along  $L$ . Let the support of  $f(t)$  on  $L$  be  $[c_1, c_2]$ , the interval of the ROI on  $L$  be  $(c_3, c_4)$ , the interval of known sub-region on  $L$  be  $(c_5, c_6)$ , and these constants satisfy  $c_1 \leq c_3 \leq c_5 < c_6 \leq c_4 \leq c_2$ .

Second, the THT along each chord/PI-line inside the ROI is computed by the DBP method, which can be expressed as

$$g(t) = \frac{1}{\pi} PV \int_{c_1}^{c_2} f(s) \frac{ds}{t-s} = (H_L f)(t), \quad t \in (c_3, c_4). \quad (14)$$

By the Tricomi formula,  $f(t)$  can be recovered from its Hilbert transform  $g(t)$

$$\sqrt{(c_2-t)(t-c_1)} f(t) = C_f + \frac{1}{\pi} PV \int_{c_1}^{c_2} g(s) \sqrt{(c_2-s)(s-c_1)} \frac{ds}{s-t}, \quad (15)$$

where  $C_f = \frac{1}{\pi} \int_{c_1}^{c_2} f(t) dt$  is a known quantity (the projection along the chord).

Third, THT along each chord is inverted by the POCS method. Because Eq. (15) can not be directly used to interior problem, the POCS method is commonly used to solve  $f$  from Eq. (14). It assumes that the 1-D function  $f$  belongs to the intersection of  $J$  convex sets  $C_1, C_2, \dots, C_J$ . If the projection operators onto these convex sets are denoted as  $P_1, P_2, \dots, P_J$ , POCS can be expressed as  $f^{k+1} = P_J P_{J-1} \dots P_1 f^k$ , where  $k$  indicates the iteration time. In other words, the interior problem is essentially to find  $f(t) \in L^2(\square)$  in the intersection of the convex sets:

$$C_1 = \{f \in L^2(\square) | (Hf)(t) = g(t), t \in (c_3, c_4)\}$$

$$C_2 = \{f \in L^2(\square) | f(t) = f_0(t), t \in (c_5, c_6)\}$$

$$C_3 = \left\{ f \in L^2(\square) \left| \frac{1}{\pi} \int_{c_1}^{c_2} f(t) dt = C_f \right. \right\}$$

$$C_4 = \{f \in L^2(\square) | f(t) \geq 0, t \in [c_1, c_2]\}$$

$$C_5 = \{f \in L^2(\square) | f(t) \leq f_{\max}, t \in [c_1, c_2]\}$$

where  $f_0(t)$  and  $f_{\max}$  are the ideal image function and its upper bound, respectively. More convex sets can be introduced if additional convex constraints are available.

#### 2.4 Scheme of statistical interior tomography

As shown in Figure. 1, the proposed statistical interior tomography scheme combines the THT-based and CS-based interior reconstruction algorithms in a statistical framework. While the result of the THT-based interior reconstruction is used as the initial guess, the CS-based interior tomography is implemented to minimize the log-likelihood term and the TV term alternatively.

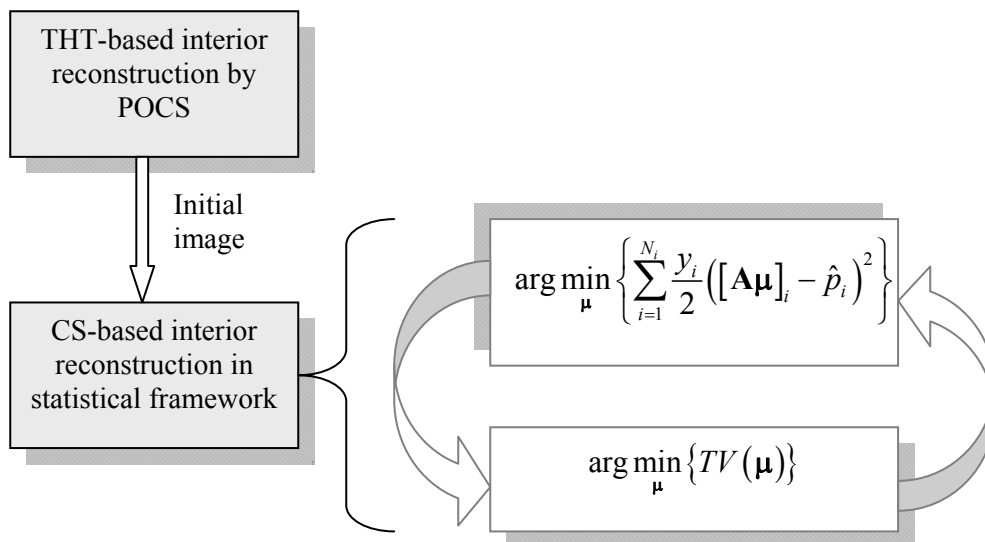


Figure.1. Scheme of the proposed statistical interior tomography

### 3. EXPERIMENTS AND RESULTS

The proposed statistical interior tomography was evaluated in both numerical simulation and practical applications.

#### 3.1 Numerical Simulation

In the numerical simulations, we used a low contrast 2-D Shepp-Logan phantom. A fan-beam geometry and an equi-spatial virtual detector were assumed. The virtual detector was centered at the system origin and always perpendicular to the line from the system origin to the x-ray source. The distance from the x-ray source to the system origin was 57 cm and the detector included 360 elements with a total length of 10.8 cm. For a full scan, we equi-angularly collected 1080 projections with  $2 \times 10^6$  photons per detector element and 360 projections with  $5 \times 10^4$  photons, respectively.

The simulated statistical interior reconstruction consists of two major steps: THT-based reconstruction and CS-based reconstruction. In the THT-based reconstruction, chords/PI- lines were constructed along the horizontal direction, and the image values on a subregion of each chord were precisely known in advance. The ROI for the THT-based reconstruction was an inscribed square inside the FOV as illustrated in Fig.2. The reconstructed images covered an FOV of radius in a  $256 \times 256$  matrix. On each chord, the ROI covered 96 pixels with a known sub-region of 6 pixels. The DBP was carried out only in the square ROI. The maximum iteration number was 500. In the CS-based reconstruction, the ROI was defined by the local scanning beam. An ordered subsets strategy was adopted to accelerate the TV minimization based SIR. The maximum iteration number was 20 with 20 subsets.

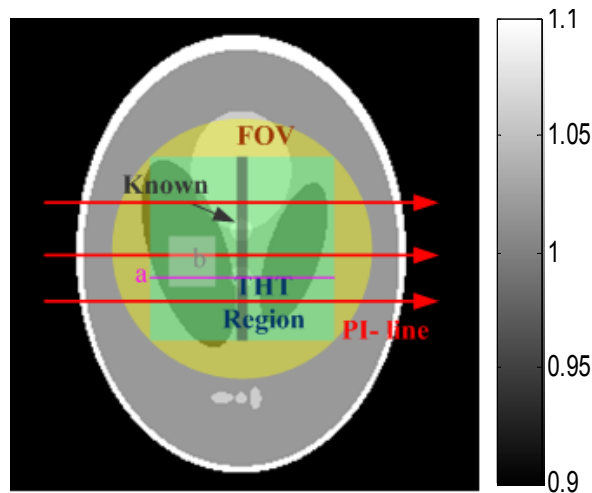


Figure. 2 The 2D Shepp-Logan phantom within a display window [0.9 1.1].

We evaluated the results of the THT-based reconstruction (denoted by THT), the CS-based statistical reconstruction initialized by a zero image (denoted by SIRCS-Zero) and the CS-based statistical reconstruction initialized by the result of the THT (denoted by SIRCS-THT). Figure. 3 showed the reconstructed images by different reconstruction schemes. It can be observed that the images reconstructed by the THT are much noisy, especially in the condition of 360 projections with  $5 \times 10^4$  photons. The noise intensity in the results reconstructed by other algorithms was lower and more stable. Moreover, the results reconstructed by SIRCS-Zero had a bias but the SIRCS-THT achieved the best performance. Representative profiles along the line *a* (see Figure.2) of the reconstructed images were shown in Figure. 4. The reconstruction accuracy of the THT was affected by the pixel position. That is, the closer to the known subregion, the more accurate the result is, which is consistent with the theoretical analysis on stability of interior tomography<sup>5</sup>. Compared to the other two schemes, THT showed much stronger noise. The SIRCS-Zero had weaker noise, but a larger bias. It may be due to several factors such as the iteration number, pixel size, image sparsify, etc. However, SIRCS-THT seems always converging to the truth.

We selected a rectangular sub-region *b* (see Figure.2) in the left ellipse with the true attenuation coefficient 0.94. The reconstructed results of the sub-region *b* using the three methods in the cases of 1080 views and  $2 \times 10^6$  photons were evaluated in Table 1 in terms of average error  $\bar{\epsilon}$ , maximum error  $\epsilon_{\max}$  and standard variation  $\sigma$ . The standard variation with THT was the largest. The bias with SIRCS-Zero was the greatest. The performance of SIRCS-THT outperformed the other two methods consistently, being the closest to the phantom image.

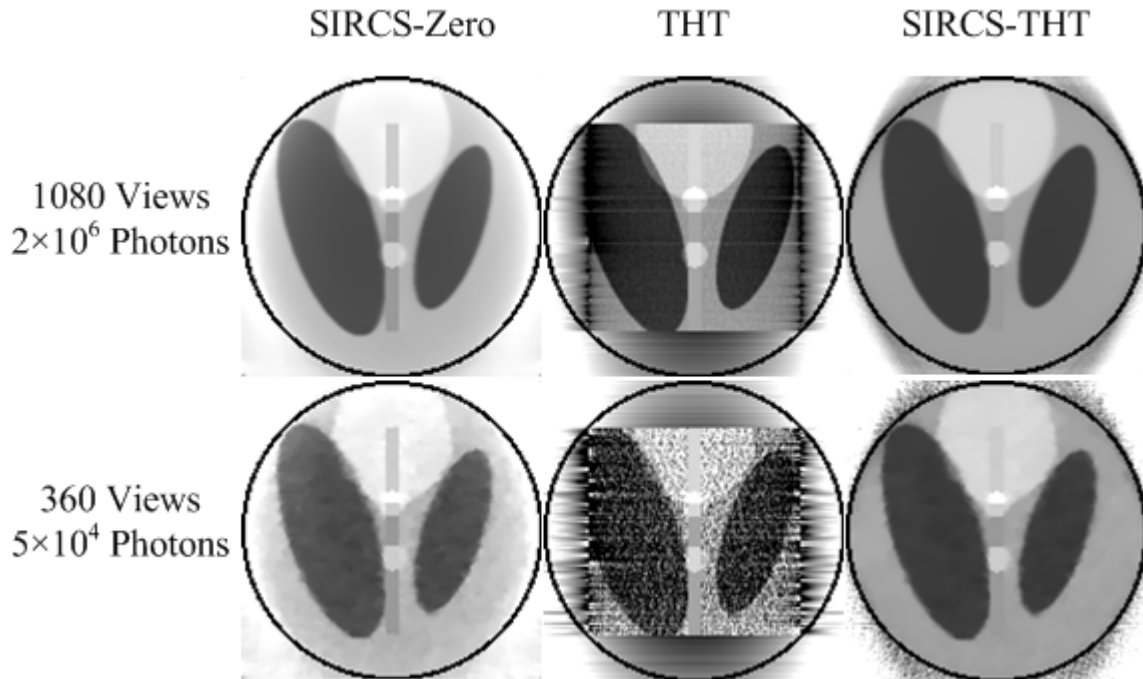


Figure 3. Images reconstructed in the ROI by the SIRCS-Zero, THT, and SIRCS-THT schemes. The display window is [0.9 1.1] for all the images.

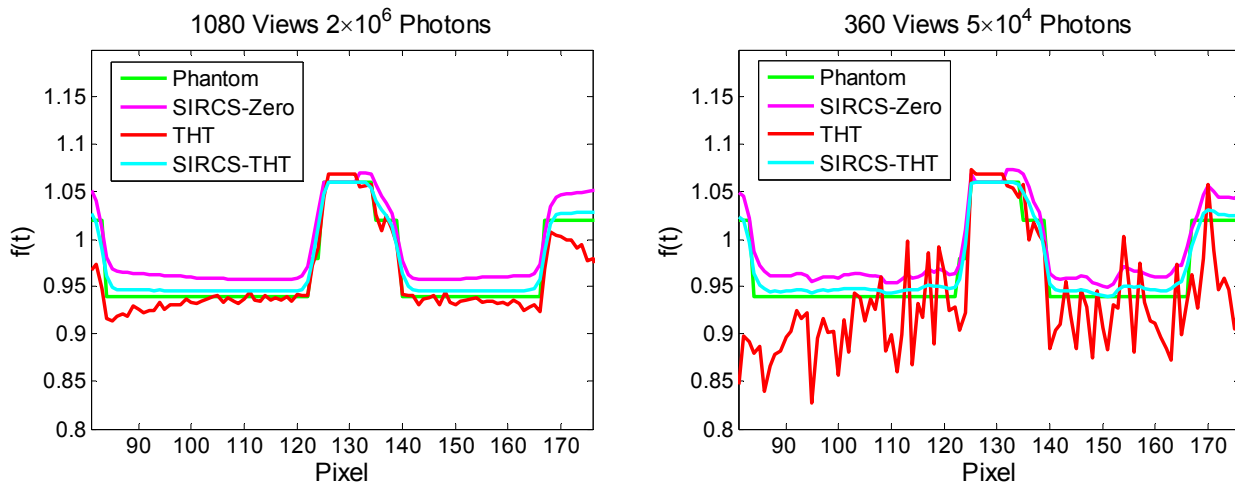


Figure 4. Profile of the reconstructed images along the line  $a$  indicated in Fig. 2. While the left is from 1080 projections and  $2 \times 10^6$  photons, the right is from 360 projections and  $5 \times 10^4$  photons.

Table 1. Comparisons of THT, SIRCS-Zero and SIRCS-THT in terms of average error, maximum error and standard deviation.

Conditions	Methods	$\bar{\varepsilon}$	$\varepsilon_{\max}$	$\sigma$
1080 Views $2 \times 10^6$ Photons	THT	0.0064	0.0266	0.0066
	SIRCS-Zero	0.0205	0.0258	0.0020
	SIRCS-THT	0.0061	0.0073	0.0004

### 3.2 Real CT data

To demonstrate the feasibility of the statistical interior reconstruction for practical applications, we performed a CT scan of a living sheep, which was approved by the University of Iowa and Virginia Tech IACUC committees. The chest of the sheep was scanned in fan-beam geometry on a SIEMENS 64-Slice CT scanner. The radius of the x-ray source scanning trajectory was 57 cm. Over a  $360^\circ$  range, 1160 projections were uniformly collected. For each projection, 672 detector elements were equi-angularly distributed to define a FOV of radius 25.05 cm. In our experiments, two scans were performed with a normal dose (100kVp, 150mAs) and a low dose (80kVp, 17mAs), respectively. We first reconstructed the entire lung cross-section in a  $512 \times 512$  matrix covering a  $29.06 \text{ cm} \times 29.06 \text{ cm}$  region from the normal dose full-scan dataset. Then, a subregion of radius 6 pixels was selected in a trachea, where the attenuation coefficient was known to be zero. After that, a circular region of radius 60 pixels around the trachea was chosen as an ROI. Finally, only the projection data through the ROI were kept to simulate an interior scan. In this situation, the PI-lines were constructed along all radial directions from the center of the trachea. The maximum iteration number of THT was fixed as 500. The maximum iteration number of the SIR was 40 with 40 subsets. Because the sheep is live, the images of the two scans at the normal and low dose levels were slightly different due to physiological motion. Therefore, the reference images were reconstructed from the corresponding full scan datasets, respectively. To improve the image quality, the reference images were reconstructed using the SIR method instead of the commonly used filtering backprojection (FBP) method.

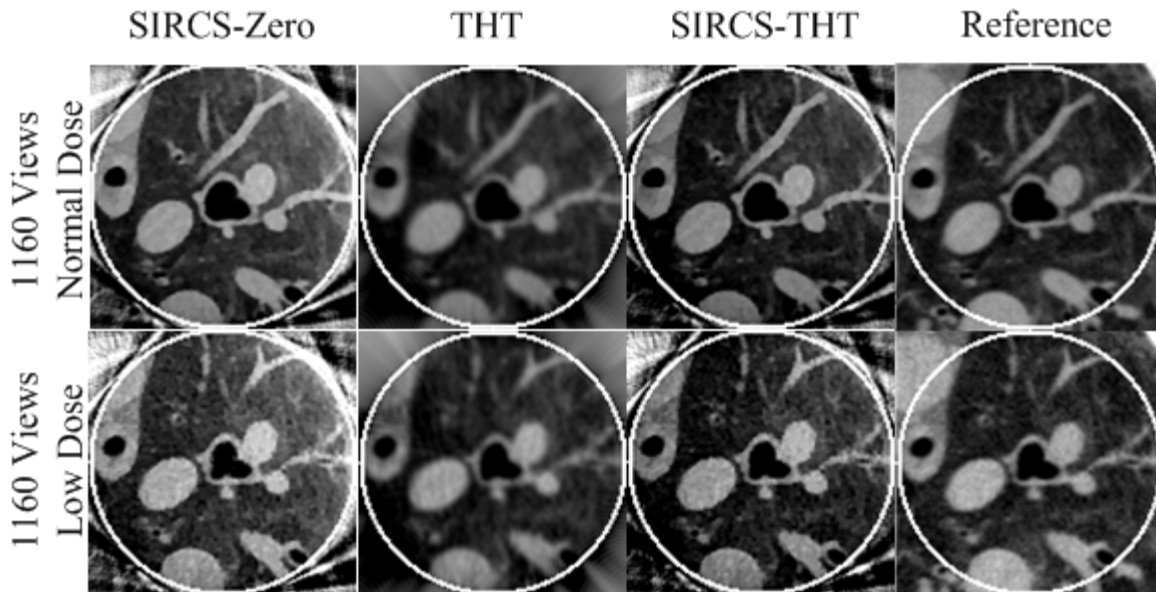


Fig. 6. Images in the ROI reconstructed by SIRCS-Zero, THT, and SIRCS-THT from normal and lose dose datasets. Display window is  $[-700\text{HU } 800\text{HU}]$  ( $1\text{HU} = 0.018/\text{mm}$ ).

Fig. 6 showed the images reconstructed by the aforementioned three reconstruction schemes with different dose levels. It can be observed that the images reconstructed by the THT have a lower spatial resolution. One reason is that the PI-lines were constructed along radial directions, and the interpolation was required for a coordinate transformation<sup>25</sup>. The results reconstructed by the other two algorithms had a higher spatial resolution and SIRCS-Zero also led to a bias as what we noticed in the numerical simulations. Typical profiles of the results were shown in Fig.7. It is noticed that while THT smoothed the image, the other two methods reserved more details. SIRCS-Zero still suffered from a substantial bias. Although the SIRCS-THT performed much better than both THT and SIRCS-Zero methods, there were still some residual artifacts especially near the peripheral region of the ROI. We are developing more sophisticated algorithms to suppress this kind of artifacts.

Because the ideal image is not known, it would be meaningless to compute the average error and standard deviation against the gold standard. Instead, we evaluated the results reconstructed with the three methods from that reconstructed from the normal dose datasets in terms of spatial resolution and an image quality assessment (IQA) index SSIM<sup>26</sup>. The results were shown in Table 2. While the SSIM measures were computed in reference of the globally reconstructed images, spatial resolution was estimated across the internal border of the trachea as the full-width-of-half-maximum

(FWHM) of the line spread function fitted into the Gaussian form<sup>27</sup>. Compared to the reference images, SIRCS-THT had the best structural similarity according to SSIM. Besides, SIRCS-THT produced a highest spatial resolution. SIRCS-Zero did not work as well as SIRCS-THT but it outperformed THT

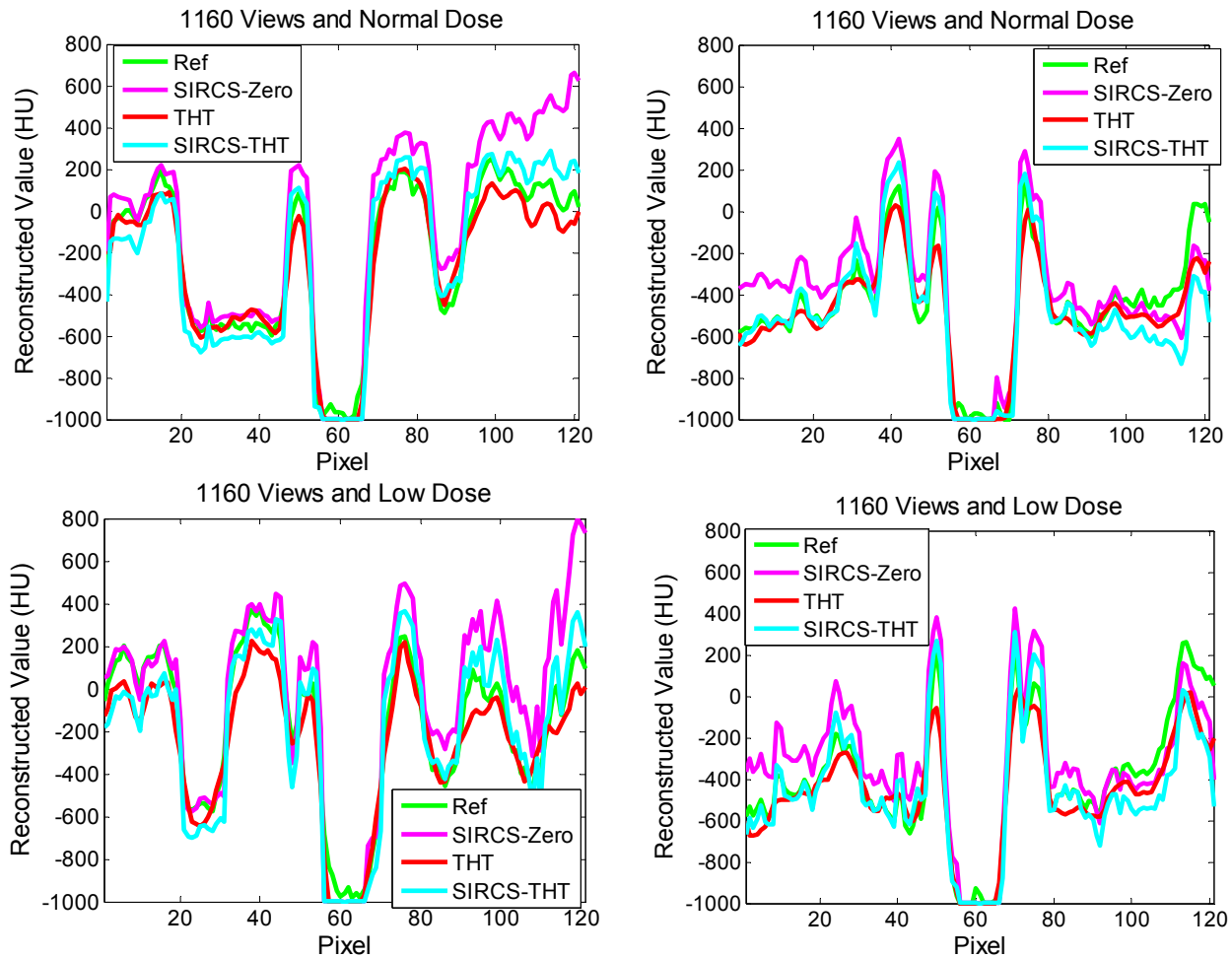


Fig. 7. Typical profile of the reconstructed results. The upper and bottom rows are respectively from normal and lose dose data. The left and right columns are respectively along the horizontal and vertical central lines of ROI.

Table 2. Comparisons of the THT, SIRCS-Zero and SIRCS-THT methods in terms of spatial resolution and SSIM.

<i>Conditions</i>	<i>Methods</i>	<i>Resolution (mm)</i>	<i>SSIM</i>
1160 Views Normal Dose	THT	2.6939	0.8423
	SIRCS-Zero	1.7688	0.8948
	SIRCS-THT	1.5967	0.9138

#### 4. DISCUSSION AND CONCLUSION

From the above experimental results, THT-based interior tomography did not have any significant bias but it is noise-sensitive. Besides, as demonstrated in Fig.4 the accuracy and robustness of this algorithm become less further away from the known subregion. Since the PI-lines are constructed around a known subregion, they are usually not consistent with

the Cartesian grid, and the involved interpolation will reduce the spatial resolution as well. On the other hand, the proposed CS-based statistical interior tomography has distinct merits in both noise and resolution aspects. In the numerical simulation, satisfactory results have been obtained even in the case of 360 views and  $5 \times 10^4$  photons. Using the IQA index SSIM to assess the results from real CT datasets, the images reconstructed using this method have produced a better structural similarity in reference to the globally reconstructed counterpart. The spatial resolution comparison has also illustrated that the proposed method has a better spatial resolution. However, TV minimization based interior tomography assumes the smooth property of ROI images, and produce suboptimal results when this assumption is significantly violated. In this regard, the high order TV (HOT) minimization approach would be a promising tool<sup>17</sup>. Additionally, this algorithm must be stopped after finitely many iterations. Hence, SIRCS with a zero initial image usually leads to a biased result. When the THT result is used as an initial guess, SIRCS has been shown to arrive at a globally optimal result very reliably. From another point of view, the THT based initialization adds the Hilbert constraint, which incorporates the known subregion into the final result. Therefore, the SIRCS-THT method not only has a strong anti-noise power and better structural details but also it is capable of eliminating any potential bias effectively.

In conclusion, we have proposed a statistical interior tomography approach by combining THT-based interior tomography, CS-based interior tomography and a statistical reconstruction framework. Our simulation and experiments have shown that it is a powerful and useful tool for local CT reconstruction in practice application.

### ACKNOWLEDGEMENT

This work is partially supported by NSFC (No. 60551003), the program of Chinese Ministry of Education (No. 20060698040, NCET-05-0828), NSF/MRI program (CMMI-0923297), and NIH/NIBIB grants (EB002667, EB011785).

### REFERENCES

- [1] Natterer, F., [The mathematics of computerized tomography] Society for Industrial Mathematics, (2001).
- [2] Maass, P., "The interior Radon transform," *SIAM Journal on Applied Mathematics*, 52(3), 710-724 (1992).
- [3] Louis, A. K., and Rieder, A., "Incomplete data problems in X-ray computerized tomography," *Numerische Mathematik*, 56(4), 371-383 (1989).
- [4] Yu, H. Y., Ye, Y. B., and Wang, G., "Interior tomography: theory, algorithms and applications," *Proc. SPIE*, 7078, 70780F (2008).
- [5] Ye, Y. B., Yu, H. Y., Wei, Y. C. *et al.*, "A general local reconstruction approach based on a truncated Hilbert transform," *International Journal of Biomedical Imaging*, Article ID:63634, 8 (2007).
- [6] Ye, Y. B., Yu, H. Y., and Wang, G., "Exact interior reconstruction with cone-beam CT," *International Journal of Biomedical Imaging*, Article ID:10693, 5 (2007).
- [7] Ye, Y. B., Yu, H. Y., and Wang, G., "Exact interior reconstruction from truncated limited-angle projection data," *International Journal of Biomedical Imaging*, Article ID:427989, 6 (2008).
- [8] Yu, H. Y., Ye, Y. B., and Wang, G., "Interior reconstruction using the truncated Hilbert transform via singular value decomposition," *Journal of the X-Ray Science and Technology*, 16(4), 243-251 (2008).
- [9] Kudo, H., Courdurier, M., Noo, F. *et al.*, "Tiny a priori knowledge solves the interior problem in CT," *Physics in Medicine and Biology*, 53, 2207-2231 (2008).
- [10] Courdurier, M., Noo, F., Defrise, M. *et al.*, "Solving the interior problem of computed tomography using a priori knowledge," *Inverse Problems*, 24, 065001 (2008).
- [11] Gelfand, I. M., and Graev, M. I., "Crofton's function and inversion formulas in real integral geometry," *Functional Analysis and Its Applications*, 25(1), 1-5 (1991).
- [12] Noo, F., Clackdoyle, R., and Pack, J. D., "A two-step Hilbert transform method for 2D image reconstruction," *Physics in Medicine and Biology*, 49, 3903-3923 (2004).
- [13] Defrise, M., Noo, F., Clackdoyle, R. *et al.*, "Truncated Hilbert transform and image reconstruction from limited tomographic data," *Inverse Problems*, 22, 1037-1053 (2006).
- [14] Yu, H. Y., and Wang, G., "Compressed sensing based interior tomography," *Physics in Medicine and Biology*, 54(9), 2791-2805 (2009).
- [15] Yu, H. Y., Yang, J. S., Jiang, M. *et al.*, "Supplemental analysis on compressed sensing based interior tomography," *Physics in Medicine and Biology*, 54, N425-N432 (2009).

- [16] Han, W. M., Yu, H. Y., and Wang, G., "A General Total Variation Minimization Theorem for Compressed Sensing Based Interior Tomography," *International Journal of Biomedical Imaging*, Article ID:125871, 3 (2009).
- [17] Yang, J. S., Yu, H. Y., Jiang, M. *et al.*, "High-order total variation minimization for interior tomography," *Inverse Problems*, 26, 035013 (2010).
- [18] Wang, G., Yu, H. Y., and Ye, Y. B., "A scheme for multisource interior tomography," *Medical Physics*, 36, 3575-3581 (2009).
- [19] Elbakri, I. A., and Fessler, J. A., "Statistical image reconstruction for polyenergetic X-ray computed tomography," *IEEE Transactions on Medical Imaging*, 21(2), 89-99 (2002).
- [20] Whiting, B. R., "Signal statistics in x-ray computed tomography," *Proc. SPIE*. 4682, 53-60 (2002).
- [21] Li, T., Li, X., Wang, J. *et al.*, "Nonlinear sinogram smoothing for low-dose X-ray CT," *IEEE Transactions on Nuclear Science*, 51(5 Part 2), 2505-2513 (2004).
- [22] Tang, J., Nett, B. E., and Chen, G. H., "Performance comparison between total variation (TV)-based compressed sensing and statistical iterative reconstruction algorithms," *Physics in Medicine and Biology*, 54(19), 5781-5804 (2009).
- [23] Yu, H. Y., and Wang, G., "A soft-threshold filtering approach for reconstruction from a limited number of projections," *Physics in Medicine and Biology*, 55, 3905-3916 (2010).
- [24] Wang, G., and Jiang, M., "Ordered-subset simultaneous algebraic reconstruction techniques (OS-SART)," *Journal of the X-Ray Science and Technology*, 12, 169-177 (2004).
- [25] Schondube, H., Stierstorfer, K., and Noo, F., "Evaluation of a 2D inverse Hilbert transform," *Proc. The first intl. conf. on image formation in X-ray CT*. 65-68bis (2010).
- [26] Wang, Z., Bovik, A. C., Sheikh, H. R. *et al.*, "Image quality assessment: From error visibility to structural similarity," *IEEE Transactions on Image Processing*, 13(4), 600-612 (2004).
- [27] Schlueter, F. J., Wang, G., Hsieh, P. S. *et al.*, "Longitudinal image deblurring in spiral CT," *Radiology*, 193(2), 413-418 (1994).